STRUCTURAL SCIENCE
CRYSTAL ENGINEERING
MATERIALS

ISSN: 2052-5206
journals.iucr.org/b

Structure factors and charge-density study of diamond at 800 K

Yuka Deguchi and Eiji Nishibori

Acta Cryst. (2018). B**74**, 651–659

STRUCTURAL SCIENCE
CRYSTAL ENGINEERING
MATERIALS

ISSN 2052-5206

Structure factors and charge-density study of diamond at 800 K

Yuka Deguchi[a] and Eiji Nishibori[a,b]*

[a]Graduate School of Pure and Applied Sciences, University of Tsukuba, 1-1-1 Tennodai, Tsukuba, Ibaraki 305-8571, Japan, and [b]Faculty of Pure and Applied Sciences and Tsukuba Research Center for Energy Materials Sciences, University of Tsukuba, 1-1-1 Tennodai, Tsukuba, Ibaraki 305-8571, Japan. *Correspondence e-mail: nishibori.eiji.ga@u.tsukuba.ac.jp

Received 17 July 2018
Accepted 22 October 2018

Edited by P. Macchi, University of Bern, Switzerland

Keywords: data correction; imaging-plate data; charge-density study; high statistics data.

Supporting information: this article has supporting information at journals.iucr.org/b

The structure factors of diamond were determined by synchrotron radiation X-ray powder diffraction at 800 K at $\sin\theta/\lambda \leq 2.2$ Å^{-1} reciprocal resolution. The structure factors were estimated using six powder profiles measured on beamline BL02B2 at SPring-8 (Hyogo, Japan). A high reciprocal resolution at $\sin\theta/\lambda \leq 2.2$ Å^{-1} was required to reveal the temperature dependence of the charge density, due to the high Debye temperature of $\theta_D = 1860$ K of diamond. Wide 2θ angle data with the highest counting statistics are crucial for accurate data analysis. The periodic noise of every six-pixel step was observed in the highest counting statistics imaging plate (IP) data scanned by a BAS2500 IP scanner. It was found that the noise originated from the six-sided polygonal mirror in the scanner. The intensity fluctuation at every six-pixel step was also found in the Fourier series expansion of the powder profiles. The ratio of the maximum fluctuation was estimated as 0.4% by summing all six-pixel step data. The powder profiles were corrected by multiplying the ratios. The intensity fluctuation in the background region was reduced to less than 50% of the uncorrected data. The weak 888 Bragg reflection, with an intensity of 0.005% of that of the 111 Bragg reflection at 800 K, was readily observed in the corrected data. Finally, the structure factors determined at 800 K were successfully applied to a charge-density study by multipole modelling. The reliability factors and multipole parameters at 800 K are in agreement with those at 300 K. The differences in the charge density at the bond midpoint and $\nabla^2\rho$ at the bond-critical point were less than 1% and 2%, respectively.

1. Introduction

The properties of a material are changed by thermal effects. Lattice expansion, changes in conductivity, changes in heat capacity *etc.* have been observed with increasing temperature. The properties depend on how the electrons are distributed (and shared) within a material. The temperature dependence of a charge-density study provides information on the thermal effects on the properties of a material. An X-ray charge-density study typically requires highly accurate and reliable diffraction data covering a wide region of reciprocal space. Diffraction data measured at low temperature are usually used for charge-density studies, because Bragg intensities in the high reciprocal resolution region are increased by the reduced thermal motion of the atoms. Until now, charge density under sufficiently high-temperature conditions has never been studied by full-parameter multipole refinement owing to the unavailability of high reciprocal resolution data. The development of measurement, data-processing and analytical techniques for charge-density studies at high temperature is highly desirable in the field of materials science. Typical materials suitable for such development are required for this purpose.

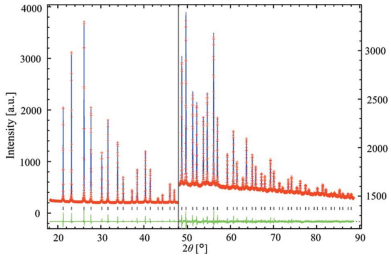

Diamond is one of the most suitable materials for charge-density studies at high temperature. Bragg peaks at high reciprocal resolution at high temperature can be observed due to the high Debye temperature of θ_D = 1860 K in the case of diamond (Victor, 1962). To date, several charge-density studies of diamond have been carried out (Brill, 1950; Carpenter, 1960; Dawson, 1967; Stewart, 1973; Takama *et al.*, 1990; Spackman, 1991; Yamamoto *et al.*, 1996; Zou & Bader, 1994; Abramov & Okamura, 1997; Nishibori *et al.*, 2007; Svendsen *et al.*, 2010; Fischer *et al.*, 2011; Bindzus *et al.*, 2014) since the possibility of charge-density studies of diamond was first demonstrated by Bragg & Bragg (1913). We also carried out an accurate charge-density study of diamond using multiple overlaid powder diffraction profiles during the past decade: powder data with $d > 0.34$ Å were used for a charge-density study by the maximum entropy method (Sakata & Sato, 1990) and multipole refinements (Nishibori *et al.*, 2007; Svendsen *et al.*, 2010; Fischer *et al.*, 2011).

The transmission Debye–Scherrer geometry and a high-temperature gas-flow device for capillary samples enable the measurement of high-quality powder data at high temperature. Weak Bragg intensities in the high-angle region at high temperature can be measured by the multiple overlaid powder profile technique (Nishibori *et al.*, 2007). There is additional scattering in the high-angle region at high temperature, such as Compton scattering and thermal diffuse scattering. The signal-to-noise ratio in the high-angle region decreases due to the increase in scattering. The multiple overlaid powder profile technique can improve the statistics of the high-angle region by changing the measurement-angle region and increasing the exposure time of the X-rays.

In the present study, we measured the powder profiles of diamond at 800 K with a high reciprocal resolution of $\sin\theta/\lambda \leq 2.2$ Å^{-1} to reveal the charge-density distribution by full-parameter multipole refinement. During the analysis process, we found systematic noise in the highest statistics imaging-plate (IP) data. By correcting the noise, we were able to use weak reflections with a high reciprocal resolution of $\sin\theta/\lambda \leq 2.2$ Å^{-1} for the charge-density study. The thermal diffuse scattering at $\sin\theta/\lambda \simeq 2.2$ Å^{-1} resolution was also observed in the corrected data. In this paper, we have determined the structure factors and charge density from the corrected data at 800 and 300 K.

2. Experimental

Multiple overlaid powder profiles of diamond were measured on beamline BL02B2 at SPring-8, Hyogo, Japan (Nishibori *et al.*, 2001; Kawaguchi *et al.*, 2007). We used an IP detector in the present study as it is still considered to be the best system in the field of charge-density studies. The suitability of the combination of an IP and high-energy X-rays at SPring-8 for charge-density studies of inorganics was confirmed by a study of $CoSb_3$ (Schmøkel *et al.*, 2013). IP detectors have also been used in powder diffractometers for charge-density studies, such as the large Debye–Scherrer camera at SPring-8 (Nishibori *et al.*, 2001) and the Aarhus vacuum imaging-plate diffractometer (Straasø *et al.*, 2013; Tolborg *et al.*, 2017). High-quality charge-density studies have been carried out and detailed charge-density distributions of TiS_2 (Kasai *et al.*, 2018), LaB_6 (Kasai & Nishibori, 2017), Si (Wahlberg *et al.*, 2016) and BN (Wahlberg *et al.*, 2015) have been revealed using IP systems. One of the advantages of the IP detector is its high counting efficiency for high-energy X-rays.

The measurement temperatures for an accurate charge-density study were determined by a preliminary measurement of the temperature-dependence powder profiles. We measured the powder profiles of diamond at temperatures of 30, 100, 200, 300, 400, 600, 800, 950 and 1100 K using N_2 and He gas-flow temperature devices. We used a Lindemann glass capillary with an internal diameter of 0.4 mm for the 30, 100, 200, 300, 400, 600 and 800 K data, and a quartz capillary with an internal diameter of 0.4 mm for the 950 and 1100 K data. The background scattering of the quartz capillary was nearly twice that of the Lindemann capillary, so the data were not suitable for an accurate charge-density study due to the low signal-to-noise ratio. The Bragg intensity of the 840 reflection at a reciprocal resolution of $\sin\theta/\lambda$ = 1.25 Å^{-1} did not change on

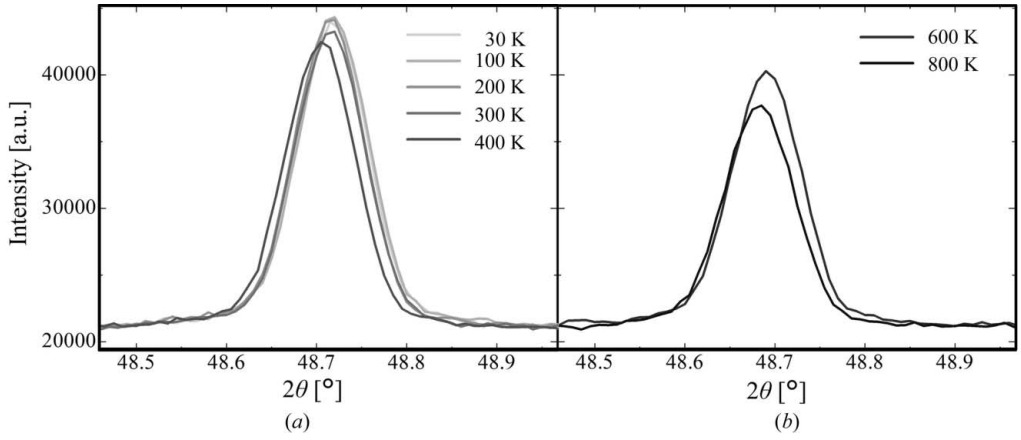

Figure 1
The temperature dependence of the powder profiles of diamond. The 840 reflections with d = 0.40 Å at (*a*) 30, 100, 200, 300, 400 and (*b*) 600 and 800 K are shown. Panel (*a*) shows that the intensity and position of the 840 reflection did not change on changing the temperature from 30 to 400 K. Panel (*b*) shows the changes in the intensity and position at 600 and 800 K.

changing the temperature from 30 to 400 K, as shown in Fig. 1. The change in the lattice constants between 30 and 400 K was less than 0.0004 Å. We selected 300 and 800 K for our accurate charge-density study because at 300 K a temperature device is not needed. Thus, the ice problem can be avoided in the low-temperature measurement. Our previous study showed that the charge density at 300 K is nearly identical to that at 100 K (Nishibori *et al.*, 2007). We were able to use a Lindemann glass capillary below 800 K to avoid melting and/or bending of the capillary as the melting point of the Lindemann glass is 858 K. We roughly estimated the Debye temperature of the present sample using the 300, 600 and 800 K data, and obtained a value of θ_D = 2000 (100) K, which is consistent with the reported value (Victor, 1962).

The wavelength of the incident X-rays was 0.3278 Å, which was calibrated using the National Institute of Standards and Technology (NIST, Maryland, USA) CeO_2 standard sample. BAS-MS IP from Fujifilm (size 40 mm × 20 mm) was used for the measurement and BAS2500 from Fujifilm was used as an IP scanner. We measured three two-dimensional powder patterns for each temperature point. The temperature of the sample was controlled at 800 and 300 K by an N_2 gas-flow high-temperature device. The 2θ ranges and exposure times of the data were 0–77° and 20 min, 18–96° and 80 min, and 34–112° and 320 min. We produced two one-dimensional powder profiles from one two-dimensional pattern by integrations of 51 and 401 pixels perpendicular to the 2θ direction. The details of the procedure were described in our previous study (Kasai & Nishibori, 2016). We denote the data sets with 20 min X-ray exposure and 51 and 401 pixel integrations as the first and second data sets, respectively. The data sets with 80 min X-ray exposure and 51 and 401 pixel integrations are denoted the third and fourth data sets, respectively. The data sets with 320 min X-ray exposure and 51 and 401 pixel integrations are denoted the fifth and sixth data sets, respectively.

Fig. 2 shows the six powder profiles at 300 and 800 K. The powder profiles of the first data set are shown in Fig. 2(*a*). The black and grey profiles are almost identical in the first five reflections and are completely overlapping. Fig. 2(*b*) shows the second data set. The peak intensities around 2θ = 46° of the 800 K data are more than 80% of those of the 300 K data. Fig. 2(*c*) shows the third data set. The second reflection here is the 222 forbidden reflection. The temperature dependence of the forbidden reflection can be readily observed in the figure. The intensities around 2θ = 70° of the 800 K data are still more than 50% of those of the 300 K data of the fourth data set shown in Fig. 2(*d*). Fig. 2(*e*) shows the fifth data set. The intensity changes at 800 K can be seen. An obvious difference can be observed for $2\theta > 90°$ of the sixth data set, as shown in Fig. 2(*f*). The intensities of the 800 K data become less than 50% of those at 300 K in this region. The highest reciprocal resolution achieved in the powder data was $\sin\theta/\lambda > 2.2$ Å^{-1} (Göttlicher & Wölfel, 1959; Nishibori *et al.*, 2007; Svendsen *et al.*, 2010; Fischer *et al.*, 2011; Bindzus *et al.*, 2014). In this region, it is difficult to see the Bragg peaks of the 800 K data due to the background noise. The noise of the diffraction data is composed of random and systematic noise. We investigated the origin of the noise using the 800 K data.

Fig. 3 shows the powder profiles and intensity histograms in the background regions at 800 K. The histograms were

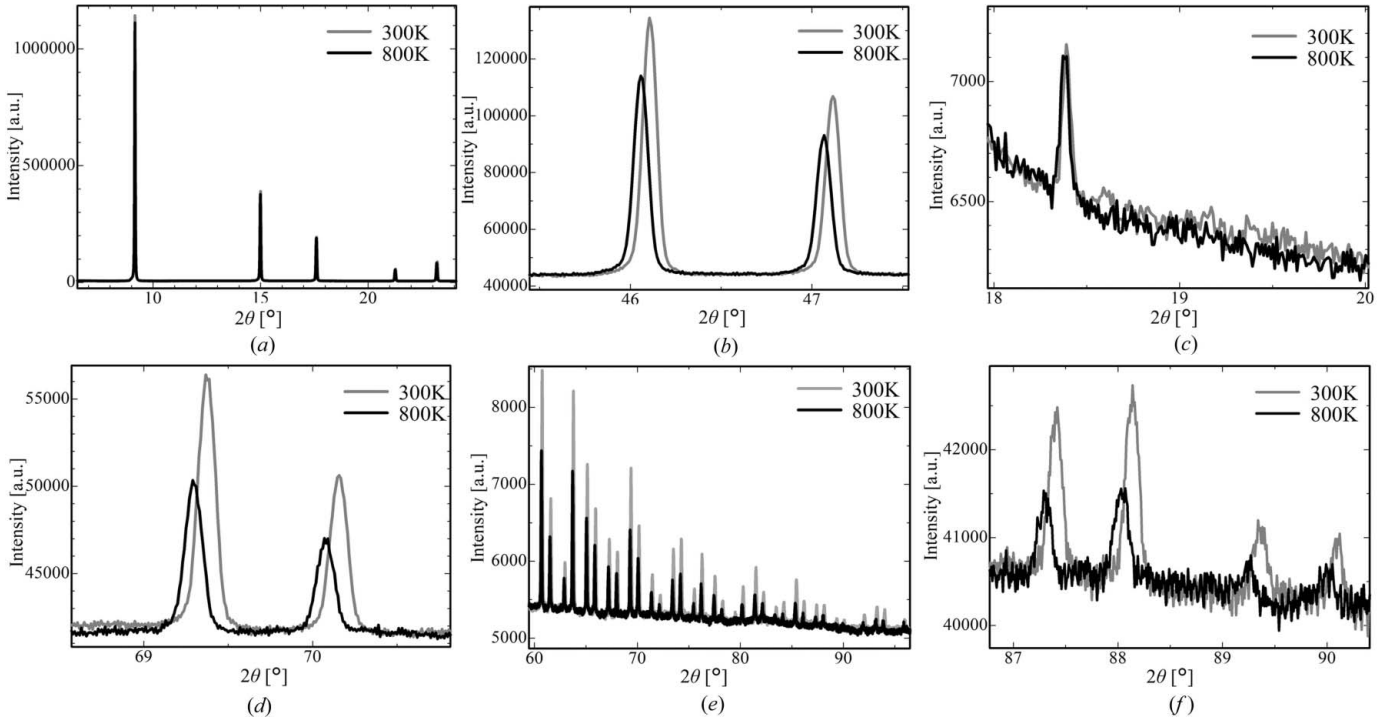

Figure 2
The six powder profiles recorded at 300 and 800 K. (*a*) First data set, (*b*) second data set, (*c*) third data set, (*d*) fourth data set, (*e*) fifth data set and (*f*) sixth data set at 300 K and 800 K. Changes in intensities are readily seen in the high-angle region.

produced using only the background intensities by removing Bragg reflection regions as indicated by black circles. We estimated the standard deviations of the histograms, which should obey a Poisson distribution if they originate only from random noise. The histograms of the first, second and third data sets can be expressed as single Gaussian peaks, as shown in Figs. 3(*a*), 3(*b*) and 3(*c*). Random noise is dominant in these data. The histograms became broader with increasing size of the data sets. There are two peaks in the histograms with the sixth data set. The profiles and histograms at 300 K also show similar features, as discussed in Section S1 in the supporting information.

Fig. 4 shows plots of the background-count dependence of the ratios between the estimated and ideal standard deviations at 800 and 300 K. The ratios are distributed around 1.0 ± 0.6 from the first to the fifth data sets. The ratio of the sixth data set is nearly 2.0 at 300 K and greater than 2.0 at 800 K, which indicates the existence of systematic noise. We further analysed the noise of the background scattering of the sixth data set.

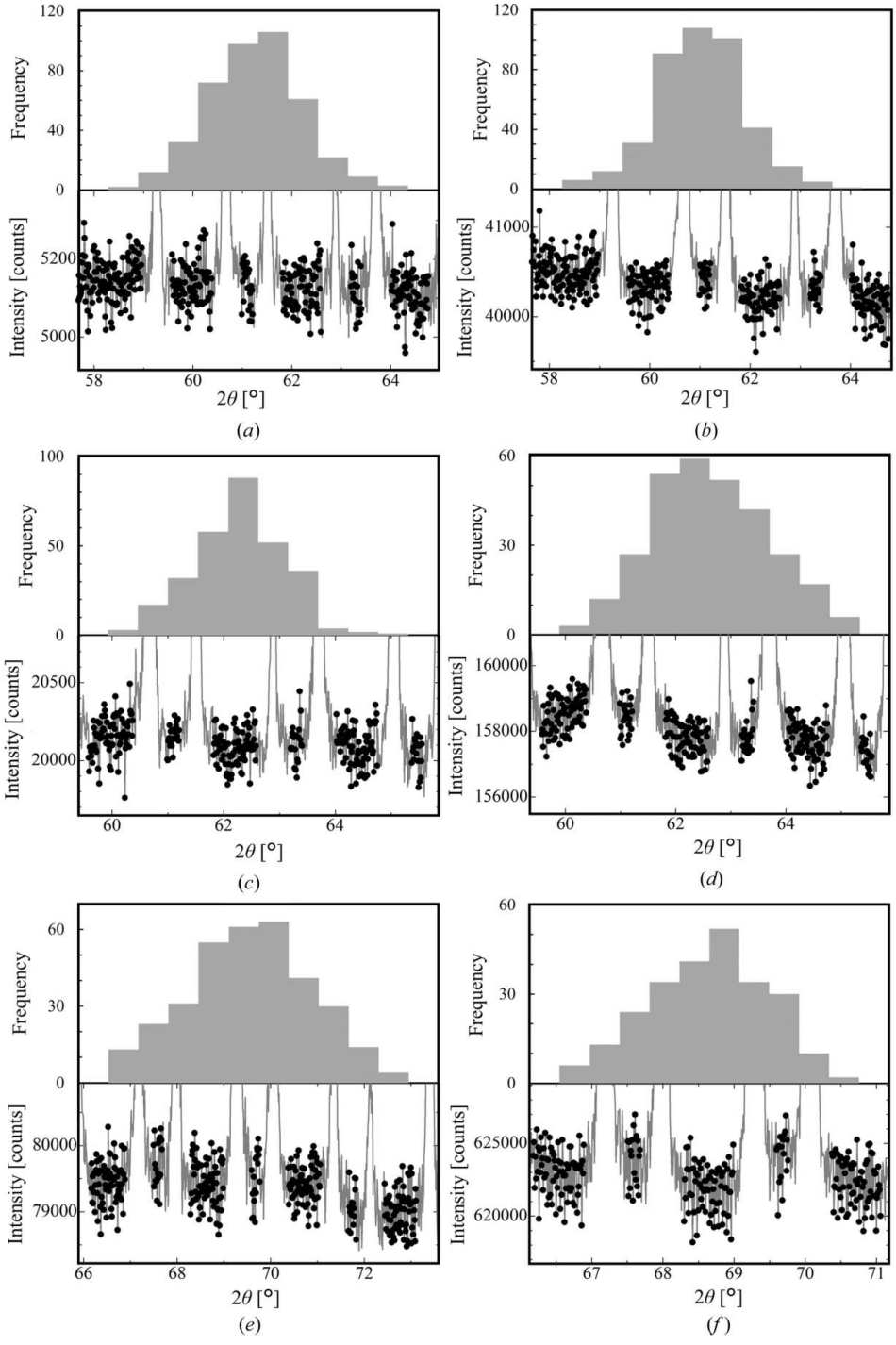

Figure 3
Powder profiles in the background region and intensity histograms of the background region at 800 K. (*a*) First, (*b*) second, (*c*) third, (*d*) fourth, (*e*) fifth and (*f*) sixth data set. The histogram of the sixth data set deviates from a single Gaussian.

3. Data correction of the highest counting statistics data

Fig. 5 shows the Fourier series expansion of the sixth powder profile at 800 K. A total of 7849 data points were used in the calculation. Apparently, there are no peaks when $n > 1000$. The insets of the figure show the expanded region around 1300. There is a sharp peak at $n = 1308$, which corresponds to a six-data-point step. We found that there was a six-point-step periodic noise in the IP data read by the BAS2500. The Fourier series expansion of the sixth powder profile at 300 K also showed peaks at 1308 in both the cosine and sine terms, as shown in Figs. S2(*a*) and S2(*b*) in the supporting information.

A six-sided polygonal mirror was used as a guide for the laser beam in the BAS2500 scanner. The shift and tilt of the mirror from the ideal position results in an intensity fluctuation at every six-point period. The difference in reflectivity between mirrors also results in the same type of fluctuation. We also calculated the Fourier series expansion of the first, second, third, fourth and fifth data sets. We could not observe a peak indicating a six-point-step periodic noise, as shown in Figs. S2(*c*) and S2(*d*) in the supporting information. The ratios between the standard deviation and

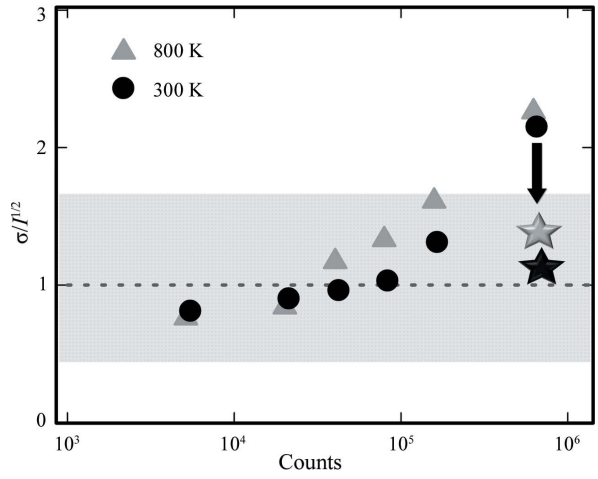

Figure 4
The dependence of the ratios between the estimated and ideal standard deviations on the background counts at 800 and 300 K. The improvement in the ratios due to the correction is shown as star symbols.

the background intensity of the first, second, third, fourth and fifth data sets are larger than 0.5%, which indicates that the intensity fluctuation is less than 0.5%.

We summed up the background region of the sixth data set at every six-data-point step. Fig. 5(*c*) shows plots of the total counts at every six-point step at 800 and 300 K. An intensity modulation of less than 0.5% can be seen in Fig. 5(*c*). The fluctuations are significantly larger than the random error, as indicated in Fig. 5(*c*). We also calculated the sum of every six-point step of the background region for the first, second, third, fourth and fifth data sets. The random errors of the sums are larger than the intensity fluctuations, as shown in Fig. S2(*e*) in the supporting information. We found that data correction for the systematic error was required only for the sixth data set. The data correction was carried out by multiplying every sixth data points by 1.004, 0.999, 1.002, 0.997, 1.000 and 0.998 at 800 and 300 K.

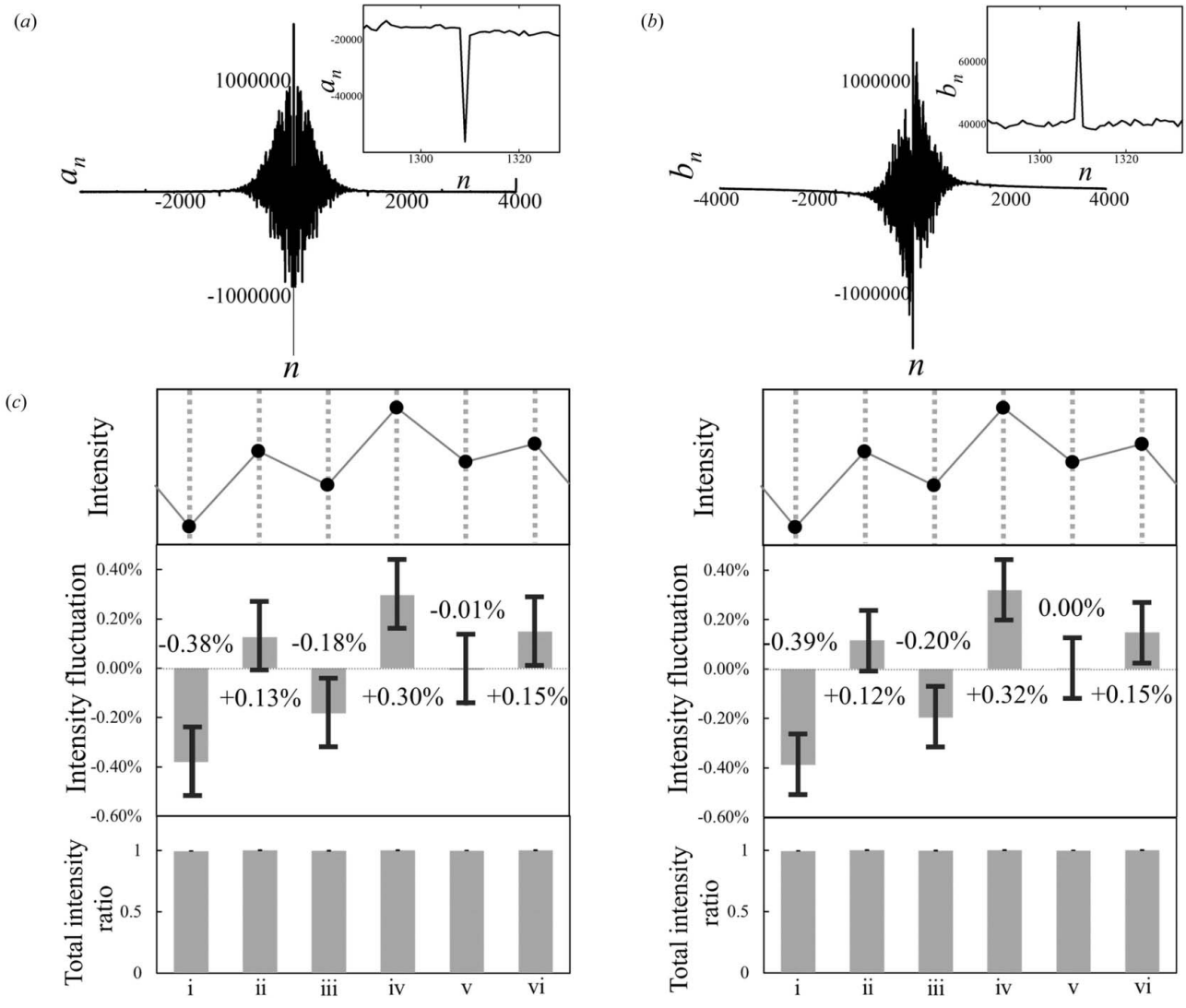

Figure 5
The amplitudes of (*a*) the cosine term and (*b*) the sine term for the Fourier series expansion of the sixth powder profile at 800 K. (*c*, top) Raw data, (middle) the intensity fluctuation ratio from the average values and (bottom) the sum of the background counts, at (left) 800 K and (right) 300 K. An intensity modulation of less than 0.5% can be seen in panel (*c*). The fluctuations were significantly larger than the random error, as indicated in panel (*c*).

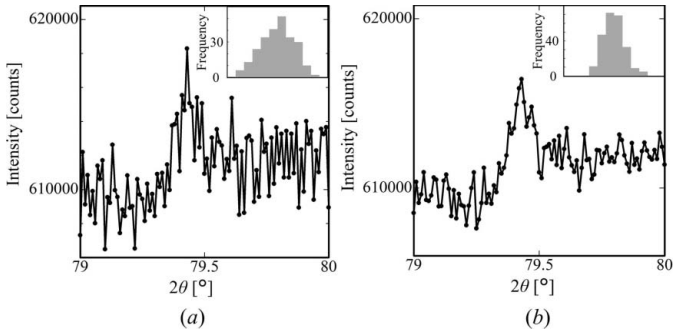

Figure 6
Powder profiles of the 888 Bragg reflections for (*a*) the uncorrected data and (*b*) the corrected data at 800 K. The insets show the intensity histograms of the background regions. The noise reduction due to the correction is clearly shown in panel (*b*).

Figs. 6(*a*) and 6(*b*) show the 888 reflections of the uncorrected and corrected data, respectively. The intensity fluctuation of the corrected data in the background region is less than 50% of that of the uncorrected data. The fluctuations were estimated using intensity histograms, which are shown in the insets of Figs. 6(*a*) and 6(*b*). The ratios of the standard deviations and intensities at 300 and 800 K are plotted as star symbols in Fig. 4. The shape of the histogram was changed to a single peak by the correction and the ratio approached random noise. These facts suggest that the correction does effectively improve the accuracy of the data. Rietveld refinements were performed on both the uncorrected and corrected data for further confirmation. The results are shown in Fig. 7 and discussed in Section S3 in the supporting information.

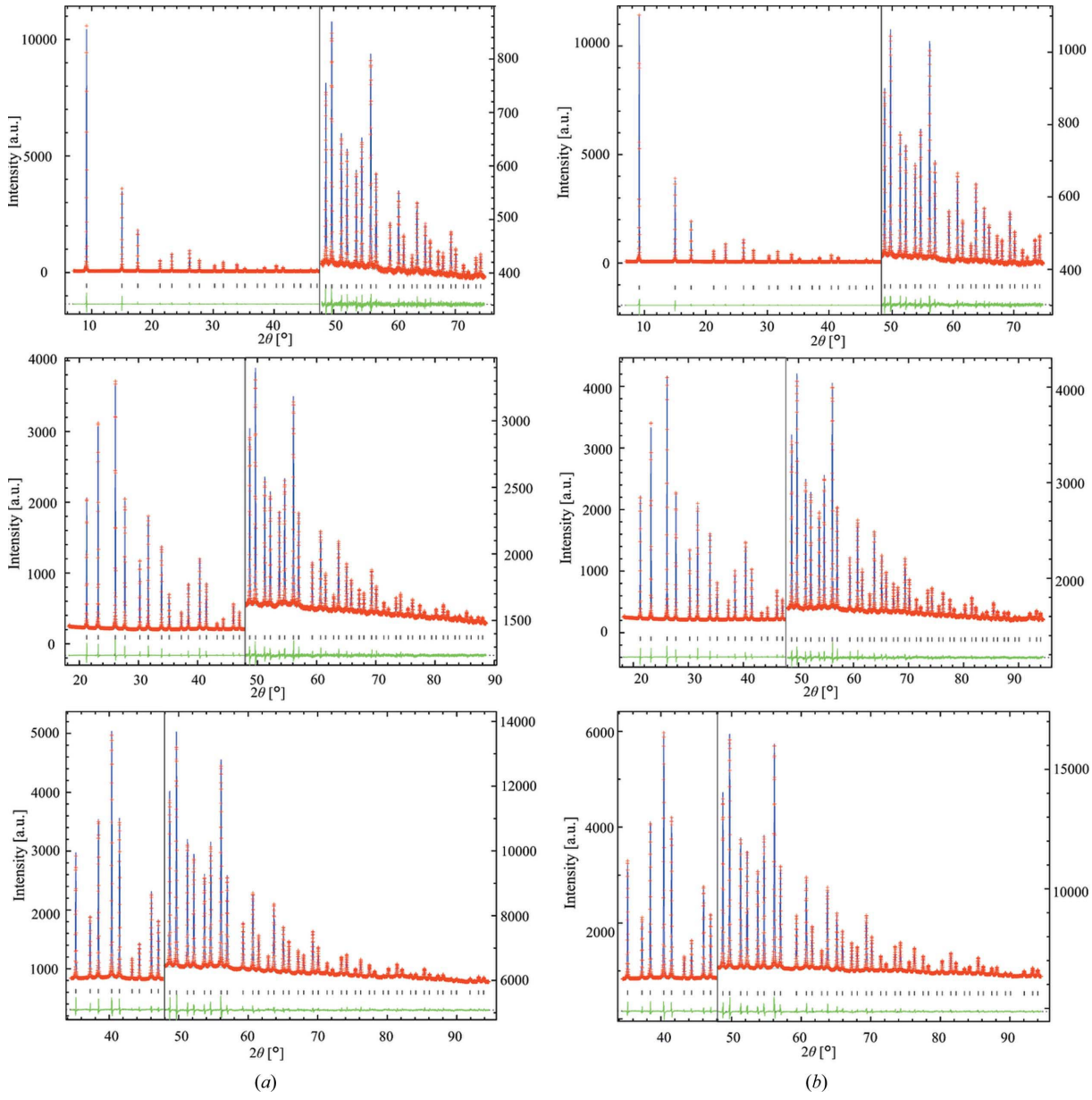

Figure 7
Results of the final profile fittings for (*a*) the 800 K data and (*b*) the 300 K data. Two data sets for each temperature are included in each frame.

Table 1
The values of R_{wp} and R_I for all six data sets and each powder profile at 800 K and 300 K.

Data	R_{wp} 800 K	R_I 800 K	R_{wp} 300 K	R_I 300 K
First	0.04450	0.00771	0.04419	0.00463
Second	0.00708	0.01946	0.00745	0.02233
Third	0.02294	0.01705	0.02204	0.01260
Fourth	0.00555	0.01903	0.00595	0.02239
Fifth	0.01189	0.01766	0.01211	0.01529
Sixth	0.00469	0.02142	0.00569	0.01933

These results confirmed that the correction has effectively improved the data analysis.

4. Structure factors and charge-density study of diamond at 800 K

The charge density was determined by multipole modelling assisted by Rietveld refinement. The details of the procedure have been described elsewhere (Svendsen *et al.*, 2010; Kasai & Nishibori, 2017). Figs. 7(*a*) and 7(*b*) show the fitting results of the final refinements at 800 and 300 K, respectively. The reliability factors of the weighted profiles, R_{wp}, and Bragg intensities, R_1, for all six data sets and each powder profile are listed in Table 1. The R_{wp} and R_i values for the sixth data set at 800 K were as small as 0.0047 and 0.0214, respectively, which are suitable for an accurate charge-density study. The reliability factors of the analysis at 800 K were comparable with those at 300 K because the standard deviations of the data sets at 800 K were the same as those of the data sets at 300 K, as shown in Table 1.

Table S1 in the supporting information provides a list of structure factors at 800 K determined in the present study. The structure factors at 300 K in the present study and in previous studies (Brill, 1950; Göttlicher & Wölfel, 1959; Nishibori *et al.*, 2007; Svendsen *et al.*, 2010; Fischer *et al.*, 2011; Bindzus *et al.*, 2014) are also shown for comparison. The total number of structure factors was 104, which is more than twice that in previous studies. The differences between the present and previous data sets are discussed in Section S4 in the supporting information. There were 90% more factors in $\sin\theta/\lambda < 1.1$ Å^{-1} at 800 K than at 300 K, suggesting that the contribution from thermal diffuse scattering is very small in the diffraction data in this region. The shape of the background scattering at 800 K in $\sin\theta/\lambda < 1.67$ Å^{-1} completely overlaps that at 300 K. The factors around $\sin\theta/\lambda \simeq 2.2$ Å^{-1} at 800 K were 60–75% of those at 300 K. The contributions from the thermal diffuse scattering in this region can be seen in Fig. S3(*d*). The determined structure factors were in good agreement with the observed background scattering.

A charge-density study was carried out using multipole refinement and Bader's topological analysis (Bader, 1990). We used multipole modelling based on the Hansen–Coppens (HC) formalism using the program *XD* (Volkov *et al.*, 2016). The relativistic C scattering factor in the Su, Coppens and Macchi (SCM) scattering databank (Su & Coppens, 1998; Macchi & Coppens, 2001) was used in the analysis because of the high reciprocal resolution of $\sin\theta/\lambda \leq 2.2$ Å^{-1}. The electron configuration was $1s^2\,2s^2\,2p^2$. We set the $2s^2\,2p^2$ valence electron shell. The local axes for the carbon atom were parallel to the [100], [010] and [001] directions. The scale factor s, isotropic thermal displacement U_{iso}, and radial expansion/contraction parameters for the spherical valence κ, aspherical valence κ', octupole O2− and hexadecapole H0 parameters were refined in the analysis. The relationship between H0 and H4+ is H4+ = 0.74048 H0. We also performed a refinement of the anharmonic thermal displacement parameters, C123, D1111 and D1122. An extended Hansen–Coppens (EHC) model, including a core deformation term, has been used in several recent studies of multipole refinement for diamond (Fischer *et al.*, 2011; Bindzus *et al.*, 2014). The alternative radial function labelled C_V in the SCM *XD* databank (Su & Coppens, 1998; Macchi & Coppens, 2001) was also used in the analysis. We performed additional multipole refinements using the EHC model and the C_V radial function in the present study.

Table S2 in the supporting information shows the final parameters of the multipole modelling. The R_F and wR values of the multipole refinement in any model of the 800 K data were comparable with those of the 300 K data. The determined parameters were highly dependent on the radial function. The R_F and wR values obtained using the C_V radial function were more than 0.1% greater at 300 K than those obtained using the C function. Table 2 shows the parameter differences between the 300 and 800 K data. The O2− population at 800 K was 0.001, *i.e.* 7%, greater than that of 300 K for the same model and radial functions. The displacement parameter at 800 K is almost twice as large as that at 300 K using the same radial function, as shown in Table S2. The topological properties at the bond critical point (BCP) and bond charge concentration (BCC) (Fischer *et al.*, 2011) are also listed in Table S2. The differences in the $\rho(\mathbf{r})_{BCP}$ at 800 and 300 K were within 0.03 e Å^{-3}, which is less than 2% of the $\rho(\mathbf{r})_{BCP}$ for the same model and radial functions, as shown in Table 2. These observations suggest that the quality of the present high-temperature data is sufficient for an accurate charge-density study within an error of 2%, even in the bonding region.

Fig. S4 in the supporting information shows the total charge density, valence charge density and static deformation density maps for the 110 plane at 800 and 300 K. The overall features at 800 K are almost identical to those at 300 K. Apparently, the total charge density at 800 K is identical to that at 300 K. A population of O2− mainly contributes to bonding between the carbon atoms. The O2− population increases by approximately 7% from 300 to 800 K. The changes in these parameters were almost indistinguishable in the charge-density map.

5. Summary

In the present study, we have determined the high-temperature structure factors and the charge density of diamond at 800 K. Data correction for the noise from IP reader required

Table 2
The parameter differences between 300 and 800 K; the deviations from parameters at 800 K to those at 300 K are shown.

Model	C	C anh	C_V	C_V anh	C EHC
Δa (Å)	0.00442 (2)				
Δu^2_{iso} (Å^2)	0.0011 (2)	0.00120 (8)	0.0011 (3)	0.00118 (10)	0.0008 (9)
$\Delta\kappa$	0.002 (5)	−0.005 (7)	0.006 (7)	−0.002 (10)	−0.01 (2)
$\Delta\kappa'$	0.03 (2)	0.03 (2)	0.03 (2)	0.03 (2)	0.02 (7)
ΔO2−	0.0009 (5)	0.0011 (4)	0.0012 (7)	0.0012 (7)	0.0012 (5)
ΔH_0	0.0015 (9)	0.0014 (9)	0.0022 (15)	0.0017 (14)	0.0014 (13)
ΔP_v	0	0	0	0	−0.000 (5)
$\Delta\kappa_c$	0	0	0	0	−0.02 (15)
ΔP_c	0	0	0	0	0.000 (5)
$\Delta C123$	0	0.00009 (13)	0	0.00008 (16)	0
$\Delta D1111$	0	0.00021 (16)	0	0.00016 (17)	0
$\Delta D1122$	0	0.00009 (6)	0	0.00007 (7)	0
$\Delta\rho(\mathbf{r})_{BCP}$ (e Å^{-3})	0.018	0.022	0.026	0.024	0.018
$\Delta\nabla^2\rho(\mathbf{r})_{BCP}$ (e Å^{-5})	−0.205	−0.576	−0.402	−0.628	−0.646
$\Delta\lambda_3\rho(\mathbf{r})_{BCP}$ (e Å^{-5})	0.39	−0.02	0.45	0.03	−0.23
$\Delta\nabla^2\rho(\mathbf{r})_{BCC}$ (e Å^{-5})	−2.1	−2	−2.2	−2	−0.3

the extraction of the Bragg intensities of weak reflections at 800 K. The high-resolution data at $\sin\theta/\lambda < 2.2$ Å^{-1} enabled the study of the charge-density distribution. The changes with respect to the room-temperature data were 0.001 in the multipole population, 0.02 e Å^{-3} in the valence and static deformation density, and −0.6 e Å^{-5} in $\nabla^2\rho(\mathbf{r})_{BCP}$. These differences can be regarded as being within standard uncertainties. The charge density at 800 K is nearly the same as that at 300 K. The charge-density distribution of a material at high temperature is generally considered as a convolution of the thermal vibration of the atoms and the charge density in the ground state. As the energy of electrons is significantly higher than that of thermal vibrations, which is confirmed by the results of this study, the contribution from the vibrations to the charge density is typically ignored in the field of materials science. Highly accurate charge-density studies can provide further confirmation.

The peak top of the 888 reflection, which is the minimum Bragg intensity of the sixth data set, has fewer than 500 counts, an intensity of only 0.005% of the 111 Bragg reflection. The required dynamic range in this study is one of the widest in the field of charge-density studies. The present study has demonstrated that a data correction is required for the IP reader to detect the weak reflection at this level. Several types of area detector, such as IPs, charge-coupled devices (CCD), pixel detectors *etc.*, have been used for charge-density studies during the past couple of decades (Bolotovsky *et al.*, 1995; Martin &Pinkerton, 1998; Wenger *et al.*, 2014). Several types of data correction for charge-density studies, such as oblique incidence correction (Wu *et al.*, 2002) and flat field correction (Bergamaschi *et al.*, 2010; Thompson *et al.*, 2011), have been developed and applied to actual data. The present study suggests a more accurate and detailed data correction is required to ensure seven-digit linearity.

Photon flux densities for X-ray charge-density studies have increased rapidly during recent decades owing to progress at synchrotron radiation facilities and in X-ray optics. Diffraction data with a seven-digit dynamic range can be measured easily by such facilities and high-accuracy detector systems. The present study suggests that a wide dynamic range without systematic noise is required for charge-density studies and is probably required for the correction of every detector. The current focus of X-ray charge-density studies is the detection of weak interactions (Kasai *et al.*, 2018) and small structural changes (Kasai & Nishibori, 2017). These studies always require high-quality data, which have never been measured so far. Detectors with a wide dynamic range and linearity are indispensable for charge-density studies in the future.

APPENDIX *A*
Fourier series expansion

In this study, a Fourier series expansion was used for the analysis of systematic noise. The Fourier series expansion can be expressed in several forms by changing the coefficient and analysis range. We describe here the equations of the Fourier series expansion used in the present study.

The Fourier series expansion defined in the range of $[0,L]$ can be expressed as

$$f(x) = a_0 + 2\sum_{n=1}^{\infty}\left[a_n\cos\left(\frac{4n\pi\theta}{L}\right) + b_n\sin\left(\frac{4n\pi\theta}{L}\right)\right], \quad (1)$$

where $f(2\theta)$ are the observed intensities. The coefficients a_n and b_n can be written as

$$a_n = \frac{1}{L}\int_0^L f(x)\cos\left(\frac{2n\pi x}{L}\right)\mathrm{d}x, \quad (2)$$

and

$$b_n = \frac{1}{L}\int_0^L f(x)\sin\left(\frac{2n\pi x}{L}\right)\mathrm{d}x. \quad (3)$$

Funding information

The synchrotron experiments were performed on beamline BL02B2 at SPring-8 with the approval of the Japan Synchrotron Radiation Research Institute (JASRI) as a Partner User (Proposal No. 2017A0074). This work was supported by the Japan Society for the Promotion of Science KAKENHI (grant Nos. JP17H05328 and JP16K13660). This work was also partly supported by the SEI Group CSR Foundation and the Casio Science Promotion Foundation.

References

Abramov, Y. A. & Okamura, F. P. (1997). *Acta Cryst.* A**53**, 187–198.
Bader, R. F. W. (1990). *Atoms in Molecules - A Quantum Theory*. Oxford University Press.
Bergamaschi, A., Cervellino, A., Dinapoli, R., Gozzo, F., Henrich, B., Johnson, I., Kraft, P., Mozzanica, A., Schmitt, B. & Shi, X. (2010). *J. Synchrotron Rad.* **17**, 653–668.
Bindzus, N., Straasø, T., Wahlberg, N., Becker, J., Bjerg, L., Lock, N., Dippel, A.-C. & Iversen, B. B. (2014). *Acta Cryst.* A**70**, 39–48.
Bolotovsky, R., Darovsky, A., Kezerashvili, V. & Coppens, P. (1995). *J. Synchrotron Rad.* **2**, 181–184.
Bragg, W. H. & Bragg, W. L. (1913). *Proc. R. Soc. London Ser. A*, **89**, 277–291.
Brill, R. (1950). *Acta Cryst.* **3**, 333–337.
Carpenter, G. B. (1960). *J. Chem. Phys.* **32**, 525–527.
Dawson, B. (1967). *Proc. R. Soc. London Ser. A*, **298**, 264–288.
Fischer, A., Tiana, D., Scherer, W., Batke, K., Eickerling, G., Svendsen, H., Bindzus, N. & Iversen, B. B. (2011). *J. Phys. Chem. A*, **115**, 13061–13071.
Göttlicher, S. & Wölfel, E. (1959). *Z. Elektrochem.* **63**, 891–901.
Kasai, H. & Nishibori, E. (2016). *Phys. Scr.* **91**, 043009.
Kasai, H. & Nishibori, E. (2017). *Sci. Rep.* **7**, 41375–41383.
Kasai, H., Tolborg, K., Sist, M., Zhang, J., Hathwar, V. R., Filsø, M. Ø., Cenedese, S., Sugimoto, K., Overgaard, J., Nishibori, E. & Iversen, B. B. (2018). *Nat. Mater.* **17**, 249–252.
Kawaguchi, S., Takemoto, M., Osaka, K., Nishibori, E., Moriyoshi, C., Kubota, Y., Kuroiwa, Y. & Sugimoto, K. (2017). *Rev. Sci. Instrum.* **88**, 085111.
Macchi, P. & Coppens, P. (2001). *Acta Cryst.* A**57**, 656–662.
Martin, A. & Pinkerton, A. A. (1998). *Acta Cryst.* B**54**, 471–477.
Nishibori, E., Sunaoshi, E., Yoshida, A., Aoyagi, S., Kato, K., Takata, M. & Sakata, M. (2007). *Acta Cryst.* A**63**, 43–52.
Nishibori, E., Takata, M., Sakata, M., Tanaka, H., Muranaka, T. & Akimitsu, J. (2001). *J. Phys. Soc. Jpn*, **70**, 2252–2254.
Sakata, M. & Sato, M. (1990). *Acta Cryst.* A**46**, 263–270.
Schmøkel, M. S., Bjerg, L., Larsen, F. K., Overgaard, J., Cenedese, S., Christensen, M., Madsen, G. K. H., Gatti, C., Nishibori, E., Sugimoto, K., Takata, M. & Iversen, B. B. (2013). *Acta Cryst.* A**69**, 570–582.
Spackman, M. A. (1991). *Acta Cryst.* A**47**, 420–427.
Stewart, R. F. (1973). *J. Chem. Phys.* **58**, 4430–4438.
Straasø, T., Becker, J., Iversen, B. B. & Als-Nielsen, J. (2013). *J. Synchrotron Rad.* **20**, 98–104.
Su, Z. & Coppens, P. (1998). *Acta Cryst.* A**54**, 646–652.
Svendsen, H., Overgaard, J., Busselez, R., Arnaud, B., Rabiller, P., Kurita, A., Nishibori, E., Sakata, M., Takata, M. & Iversen, B. B. (2010). *Acta Cryst.* A**66**, 458–469.
Takama, T., Tsuchiya, K., Kobayashi, K. & Sato, S. (1990). *Acta Cryst.* A**46**, 514–517.
Thompson, S. P., Parker, J. E., Marchal, J., Potter, J., Birt, A., Yuan, F., Fearn, R. D., Lennie, A. R., Street, S. R. & Tang, C. C. (2011). *J. Synchrotron Rad.* **18**, 637–648.
Tolborg, K., Jørgensen, M. R. V., Christensen, S., Kasai, H., Becker, J., Walter, P., Dippel, A.-C., Als-Nielsen, J. & Iversen, B. B. (2017). *Acta Cryst.* B**73**, 521–530.
Victor, A. C. (1962). *J. Chem. Phys.* **36**, 1903–1911.
Volkov, A., Macchi, P., Farrugia, L. J., Gatti, C., Mallinson, P., Richter, T. & Koritsanszky, T. (2016). *XD2016*. University of Glasgow, Scotland.
Wahlberg, N., Bindzus, N., Bjerg, L., Becker, J., Christensen, S., Dippel, A. C., Jørgensen, M. R. V. & Iversen, B. B. (2015). *J. Phys. Chem. C*, **119**, 6164–6173.
Wahlberg, N., Bindzus, N., Bjerg, L., Becker, J., Dippel, A.-C. & Iversen, B. B. (2016). *Acta Cryst.* A**72**, 28–35.
Wenger, E., Dahaoui, S., Alle, P., Parois, P., Palin, C., Lecomte, C. & Schaniel, D. (2014). *Acta Cryst.* B**70**, 783–791.
Wu, G., Rodrigues, B. L. & Coppens, P. (2002). *J. Appl. Cryst.* **35**, 356–359.
Yamamoto, K., Takahashi, Y., Ohshima, K., Okamura, F. P. & Yukino, K. (1996). *Acta Cryst.* A**52**, 606–613.
Zou, P. F. & Bader, R. F. W. (1994). *Acta Cryst.* A**50**, 714–725.